The Bioscan AN INTERNATIONAL QUARTERLY JOURNAL OF LIFE SCIENCES
20(3): S.I (3), 764-775, 2025 www.thebioscan.com

Spectroscopic, Quantum Chemical, Molecular Docking and In Vitro Cytotoxicity Studies on 1-(Chloromethyl)anthraquinone: A potent Lung Cancer Drug

Hima S[1], M.R. Meera[2,*], C.Vijayakumar[3], R. Premkumar[4]

[1]Research scholar (Reg. No.21123232132004), Department of Physics, St. Jude's College, Thoothoor-629 176, Affiliated to Manonmanium Sundaranar University, Abishekapatti, Tirunelveli-627 012, Tamil Nadu, India.

[2]Department of physics, Sree Ayyappa College for Women, Chunkankadai, Nagarcoil-629003, Tamil Nadu, India.

[3]Department of Physics, St. Jude's College, Thoothoor, Kanyakumari District-629176, Tamil Nadu, India.

[4]Advanced Materials Research Centre, PG and Research Department of Physics, Nadar Mahajana Sangam S. Vellaichamy Nadar College, Nagamalai, Madurai-625019, Tamil Nadu, India.

*Corresponding Author: **Dr. M.R. Meera, Ph. D.,**

TEL: +91-9443692523

E-mail: meeranairmrm17@gmail.com

DOI: 10.63001/tbs.2025.v20.i03.S.I(3).pp764-775

KEYWORDS
1-(Chloromethyl)anthraquinone (CMAQ), Density Functional Theory, FT-IR, FT-Raman, Molecular Docking, A549 lung cancer cells, HeLa cervical cancer cells
Received on:

06-07-2025

Accepted on:

05-08-2025

Published on:

09-09-2025

ABSTRACT

In this work, a comprehensive investigation of 1-(Chloromethyl)anthraquinone (CMAQ) was carried out using a combination of spectroscopic, quantum chemical, molecular docking, and in vitro cytotoxicity approaches to evaluate its potential as an anticancer candidate. The molecular structure was optimized using Density Functional Theory (DFT) at the B3LYP/cc-pVTZ level, confirming a stable C_1 point group geometry with a HOMO–LUMO energy gap of 4.18 eV, indicative of moderate chemical reactivity and stability. Frontier molecular orbital analysis, global reactivity descriptors, Mulliken charge distribution, and Molecular Electrostatic Potential mapping revealed electron-rich carbonyl oxygen atoms as favorable electrophilic sites and a chloromethyl substituent susceptible to nucleophilic substitution. Vibrational assignments from FT-IR and FT-Raman spectra were consistent with theoretical predictions, validating the computational model. Time-dependent DFT simulations showed excellent agreement with experimental UV–Vis absorption, confirming $n \rightarrow \pi^*$ transitions characteristic of anthraquinone derivatives. Molecular docking studies demonstrated stronger binding affinity of CMAQ toward DPP-4 (−7.42 kcal/mol) compared with p38α MAPK (−6.21 kcal/mol). In vitro cytotoxicity assays revealed potent activity of CMAQ against A549 lung cancer cells (IC_{50} = 4.12 µg/mL) and moderate activity against HeLa cervical cancer cells (IC_{50} = 13.25 µg/mL), with apoptosis-like morphological changes confirmed microscopically. Overall, the integrated findings highlight CMAQ as a promising lead compound with preferential efficacy against lung cancer, supported by both computational and experimental evidence.

INTRODUCTION

Anthraquinone and its derivatives represent an important class of aromatic compounds widely used in dyes, pigments, photodynamic agents, and pharmaceutical [1,2]. The quinone scaffold, characterized by its conjugated π-system and reactive carbonyl groups, imparts unique redox properties that underpin a broad range of biological and therapeutic activities, including anticancer, antibacterial, and antiviral effects [3-5]. Structural modifications at different positions of the anthraquinone core significantly alter physicochemical behavior, intermolecular interactions, and biological profiles [6].

Among substituted anthraquinones, halogenated derivatives have gained particular attention due to the ability of halogen substituents to modulate lipophilicity, membrane permeability, and binding affinity toward biomolecular targets [7,8]. In this context,

1-(Chloromethyl)anthraquinone (CMAQ) is of considerable interest as the chloromethyl substituent introduces both an electron-withdrawing effect and a potentially reactive site, thereby influencing conjugation, charge distribution, and molecular recognition.

Recent advances in computational chemistry and spectroscopic characterization enable a deeper understanding of anthraquinone derivatives at the molecular level. Density Functional Theory (DFT) calculations provide reliable predictions of optimized geometries, vibrational frequencies, and electronic properties, while FT-IR and FT-Raman spectroscopy serve as experimental complements for vibrational assignment [9,10]. Moreover, Frontier Molecular Orbital (FMO) analysis, global

reactivity descriptors, and Molecular Electrostatic Potential (MEP) mapping allow identification of reactive sites, which are crucial for understanding ligand–target interactions.

In parallel, molecular docking studies offer a computational approach to predict the binding affinity and mode of interaction of anthraquinones with biological macromolecules, providing insights into their therapeutic potential [11,12]. Finally, in vitro cytotoxicity assays** against human cancer cell lines provide experimental validation of the predicted bioactivity, bridging the gap between theoretical modeling and biomedical applications [13].

The present work integrates spectroscopic, quantum chemical, molecular docking, and in vitro cytotoxicity studies of CMAQ with the objective of assessing its potential as a novel cervical cancer drug candidate. By combining DFT-based structural and vibrational analysis, electronic property evaluation, molecular docking simulations, and biological assays, this study aims to establish a comprehensive molecular fingerprint of CMAQ and highlight its therapeutic relevance.

2. Materials and Methods

2.1 Experimental Characterizations

The 1-(Chloromethyl) anthraquinone (CMAQ) compound, with a purity of 98%, was purchased from Sigma-Aldrich Chemicals Co. (St. Louis, MO, USA) and used without further purification. The Fourier Transform Infrared (FT-IR) spectrum was recorded at room temperature in the 4000–400 cm^{-1} region using a PerkinElmer Spectrum 1 spectrometer and the KBr pellet technique, with a spectral resolution of 1 cm^{-1}. The Fourier Transform Raman (FT-Raman) spectrum was collected with a Bruker RFS 27 spectrometer equipped with a Nd:YAG laser (1064 nm excitation), using a spectral resolution of 2 cm^{-1}. Both FT-IR and FT-Raman spectra were measured in the 3500–400 cm^{-1} region. The ultraviolet-visible (UV-Vis) absorption spectrum was obtained on a Shimadzu UV-3600 UV-Vis-NIR spectrophotometer in the range of 200–600 nm, using ethanol as the solvent.

The anticancer activity of CMAQ was evaluated by the 3-(4,5-dimethylthiazol-2-yl)-2,5-diphenyltetrazolium bromide (MTT) assay. Cytotoxicity was tested against two human cancer cell lines: A549 (human lung carcinoma) and HeLa (human cervical carcinoma). Cells were cultured in Dulbecco's Modified Eagle Medium (DMEM) supplemented with 10% fetal bovine serum (FBS) and 1% penicillin-streptomycin. CMAQ was applied at concentrations ranging from 0–360 µg/mL for 24 h. After treatment, 20 µL of MTT solution (5 mg/mL) was added to each well, followed by incubation for 4 h. Formazan crystals formed were dissolved in dimethyl sulfoxide (DMSO), and absorbance was measured at 570 nm using a microplate reader. The IC_{50} values were calculated from the dose–response curves.

2.2 Computational Details

The molecular geometry of CMAQ was optimized using Density Functional Theory (DFT) at the B3LYP/cc-pVTZ level as implemented in Gaussian 09W [14]. Frequency calculations confirmed the optimized geometry as a true energy minimum (no imaginary frequencies). Vibrational frequencies were scaled using correction factors of 0.9840 for stretching modes and bending modes [15]. Vibrational mode assignments were performed with the aid of Potential Energy Distribution (PED) analysis using the VEDA 4.0 program [16]. Electronic absorption spectra were simulated using Time-Dependent Density Functional Theory (TD-DFT) at the B3LYP/cc-pVTZ level, incorporating solvent effects (ethanol) through the Polarizable Continuum Model (PCM). Simulated absorption maxima, oscillator strengths, and electronic transitions were compared with experimental UV-Vis spectra. The frontier molecular orbitals (HOMO and LUMO), Mulliken atomic charges, and Molecular Electrostatic Potential (MEP) surfaces were visualized with GaussView 05 [17]. Global reactivity descriptors, including ionization energy, electron affinity, electronegativity, hardness, softness, and electrophilicity index, were derived using Koopmans' theorem.

2.3 Molecular Docking Studies

Molecular docking simulations were performed to predict the interaction of CMAQ with cancer-related protein targets using the AutoDock 4.0.1 software package [11]. Protein crystal structures were retrieved from the Protein Data Bank (PDB). For lung cancer studies, Dipeptidyl Peptidase-4 (DPP-4, PDB ID: 2ONC) was chosen [19], while for cervical cancer studies, p38α Mitogen-Activated Protein Kinase (MAPK14, PDB ID: 3FMK) was selected [18]. Protein structures were prepared by removing crystallographic water molecules and co-crystallized ligands, followed by the addition of polar hydrogens and Kollman charges. The CMAQ ligand was optimized at the DFT/B3LYP/cc-pVTZ level and converted into the PDBQT format for docking. The docking grid box encompassed the active site of each protein. The Lamarckian Genetic Algorithm (LGA) was employed with 100 runs, a population size of 150, and a maximum of 2.5×10^6 energy evaluations. The best docking poses were selected based on lowest binding free energy and favorable interaction profiles. Docking results were visualized using PyMOL Visualizer.

2.4 In Vitro Cytotoxicity Studies

The cytotoxic effect of CMAQ was assessed by the MTT assay against A549 and HeLa cells, following the procedure described in Section 2.1. Cell viability was expressed as a percentage relative to untreated controls. IC_{50} values were determined using nonlinear regression analysis. Morphological changes in treated cells were monitored under an inverted phase-contrast microscope, where apoptotic features such as cell shrinkage, blebbing, and detachment were observed, confirming cytotoxic action.

3. Results and Discussion

3.1 Molecular geometry and symmetry

The optimized structural parameters of the CMAQ molecule, calculated using the DFT/B3LYP method with the cc-pVTZ basis set, are summarized in Table 1, while the corresponding molecular structure is illustrated in Fig. 1. The calculated ground-state energy of the optimized CMAQ molecule was found to be –1187.475 atomic units (a.u.), indicating a stable and energetically favorable conformation. The bond lengths and bond angles reveal important insights into the geometry and electronic delocalization of the molecule. The aromatic framework of CMAQ is nearly planar, as reflected by the uniformity of the C–C bond lengths (1.39–1.41 Å) within the benzene-like ring systems. These values are in close agreement with standard aromatic C–C distances, highlighting the conjugated π-system. The C–H bond lengths (~1.08 Å) remain consistent with typical aromatic C–H distances, further validating the optimized geometry.

The substitution at C17 by chlorine (Cl18) and hydrogens (H26, H27) introduces slight deviations in bond angles around the carbon center. The C–Cl bond length (1.921 Å) is in the expected range for sp^3–Cl substitution, while the bond angles at C17 (C2–C17–Cl18 = 111.36°, C2–C17–H26 = 113.26°, C2–C17–H27 = 113.09°) are slightly widened compared to the ideal tetrahedral angle, due to the larger atomic radius and electron-withdrawing nature of chlorine. The carbonyl groups (C9–O16 = 1.2529 Å, C10–O15 = 1.2531 Å) show shorter bond lengths typical of double bonds, confirming their π-bonding nature. Bond angles around the carbonyl carbons (C11–C9–O16 = 121.21° and C12–C10–O15 = 121.22°) suggest sp^2 hybridization and planarity of the carbonyl groups, which may enhance conjugation with the aromatic system.

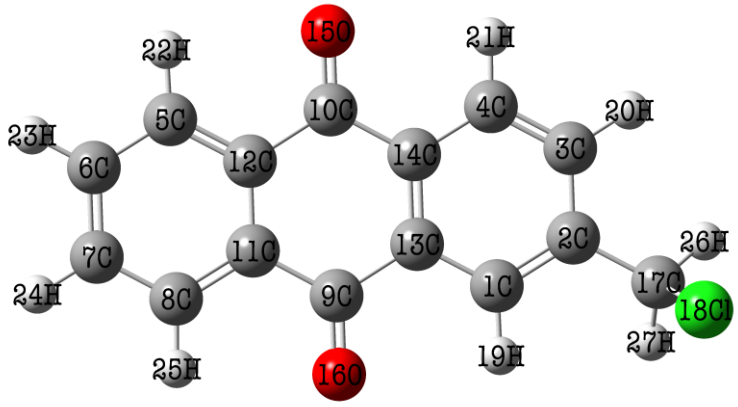

Fig.1. The optimized molecular structure of CMAQ molecule

Table 1. The optimized structural parameters of CMAQ molecule calculated by the DFT/B3LYP method with cc-pVTZ basis set.

Structural Parameters	Bond length (Å)	Structural Parameters	Bond angle (degree)
C1-C2	1.4007	C3-C4-C14	120.2638
C1-C13	1.4005	C3-C4-H21	121.3504
C1-H19	1.0849	C14-C4-H21	118.3858
C2-C3	1.4093	C6-C5-C12	120.2055
C2-C17	1.4924	C6-C5-H22	121.4415
C3-C4	1.3926	C12-C5-H22	118.3530
C3-H20	1.0856	C5-C6-C7	120.1023
C4-C14	1.4032	C5-C6-H23	119.8871
C4-H21	1.0838	C7-C6-H23	120.0105
C5-C6	1.3961	C6-C7-C8	120.1002
C5-C12	1.4027	C6-C7-H24	120.0164
C5-H22	1.0840	C8-C7-H24	119.8834
C6-C7	1.4031	C7-C8-C11	120.2021
C6-H23	1.0849	C7-C8-H25	121.4501
C7-C8	1.3961	C11-C8-H25	118.3478
C7-H24	1.0849	C11-C9-C13	117.9243
C8-C11	1.4027	C11-C9-O16	121.2097
C8-H25	1.0840	C13-C9-O16	120.8660
C9-C11	1.4837	C12-C10-C14	117.9457
C9-C13	1.4861	C12-C10-O15	121.2160
C9-O16	1.2529	C14-C10-O15	120.8383
C10-C12	1.4838	C8-C11-C9	119.2668
C10-C14	1.4854	C8-C11-C12	119.6997
C10-O15	1.2531	C9-C11-C12	121.0334
C11-C12	1.4137	C5-C12-C10	119.2837
C13-C14	1.4114	C5-C12-C11	119.6902
C17-Cl18	1.9213	C10-C12-C11	121.0261
C17-H26	1.0884	C1-C13-C9	119.2037
C17-H27	1.0879	C1-C13-C14	119.7656
Structural Parameters	**Bond angle (degree)**	C9-C13-C14	121.0306
C2-C1-C13	120.7563	C4-C14-C10	119.4150
C2-C1-H19	121.0527	C4-C14-C13	119.5498
C13-C1-H19	118.1910	C10-C14-C13	121.0352
C1-C2-C3	119.0406	C2-C17-Cl18	111.3597
C1-C2-C17	120.4177	C2-C17-H26	113.2651
C3-C2-C17	120.5416	C2-C17-H27	113.0946
C2-C3-C4	120.6233	Cl18-C17-H26	103.5256
C2-C3-H20	119.4992	Cl18-C17-H27	103.9421
C4-C3-H20	119.8764	H26-C17-H27	110.8423

3.2 Vibrational Analysis

The vibrational properties of the CMAQ molecule were analyzed using the DFT/B3LYP method with the cc-pVTZ basis set, and the results are summarized in Table 2. Owing to its C1 point group symmetry, the molecule possesses no symmetry restrictions; hence, all vibrational modes are both IR and Raman active. For the 27 atoms in CMAQ, the total number of normal modes of vibration is given by 3N - 6 = 75. Accordingly, 75 fundamental vibrational modes were obtained and assigned with the aid of potential energy distribution (PED) analysis, and their corresponding IR and Raman spectra are illustrated in Fig. 2 and Fig. 3, respectively.

The low-frequency region below 200 cm^{-1} is dominated by skeletal deformations and ring torsions, as indicated by modes 1-8. These correspond to collective lattice-like vibrations involving out-of-plane displacements of the aromatic ring system, consistent with reports for anthraquinone derivatives. The medium-frequency region (200–1000 cm^{-1}) contains several C–H out-of-plane bending and ring deformation modes (modes 9–40), with strong Raman activity observed around 535–700 cm^{-1}, characteristic of substituted quinones [19,20].

The fingerprint region between 1000 and 1700 cm^{-1} is particularly rich in C–C stretching, C–H in-plane bending, CH_2 bending, and C=O stretching vibrations. The modes at 1346, 1356, and 1387 cm^{-1} exhibit intense IR activity, which are attributed to C–C stretching coupled with C–H bending, while the band at 1399 cm^{-1} corresponds predominantly to C–C stretching. Importantly, strong bands are observed in the 1600–1670 cm^{-1} region (modes 61–66), assigned to C=O stretching vibrations of the quinone group coupled with aromatic C–C stretching, in good agreement with previously reported values for anthraquinone derivatives. The most intense IR absorption is predicted at 1346 cm^{-1} (mode 52), attributed to mixed C–C stretching and C–H bending, which also shows significant Raman scattering activity.

The high-frequency region (3100–3250 cm^{-1}) corresponds to C–H and CH_2 stretching vibrations (modes 67–75). These are characterized by very high PED contributions (>95%) from C–H stretches, with IR bands around 3200–3220 cm^{-1} and intense Raman activity, consistent with the aromatic character of CMAQ. Thus, the vibrational assignment reveals that the presence of the quinone moiety strongly influences the C=O stretching vibrations, while the aromatic ring structure gives rise to well-defined skeletal, bending, and stretching modes across the spectrum. The calculated results (Table 2) show close consistency with typical experimental data of anthraquinone derivatives, validating the reliability of the DFT method employed [21].

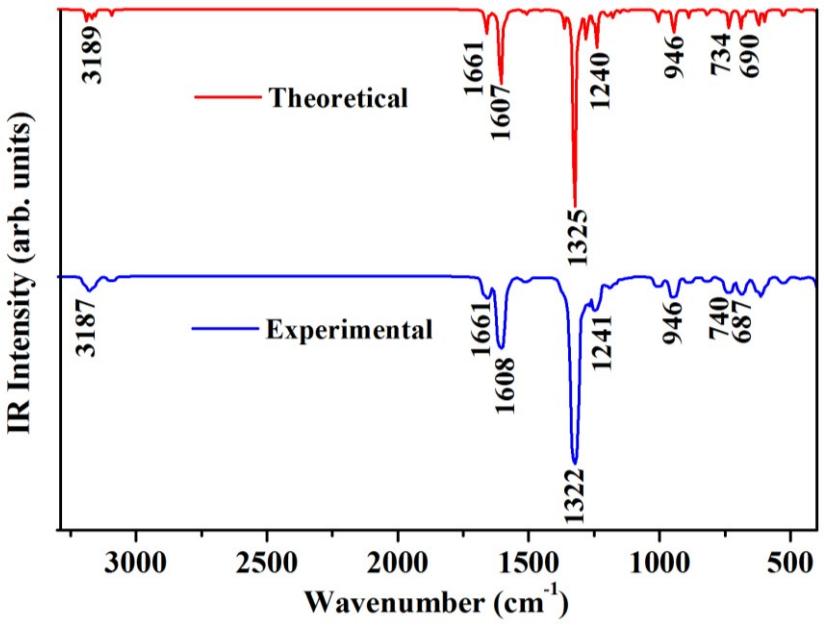

Fig.2. The simulated and observed infrared spectra of CMAQ molecule

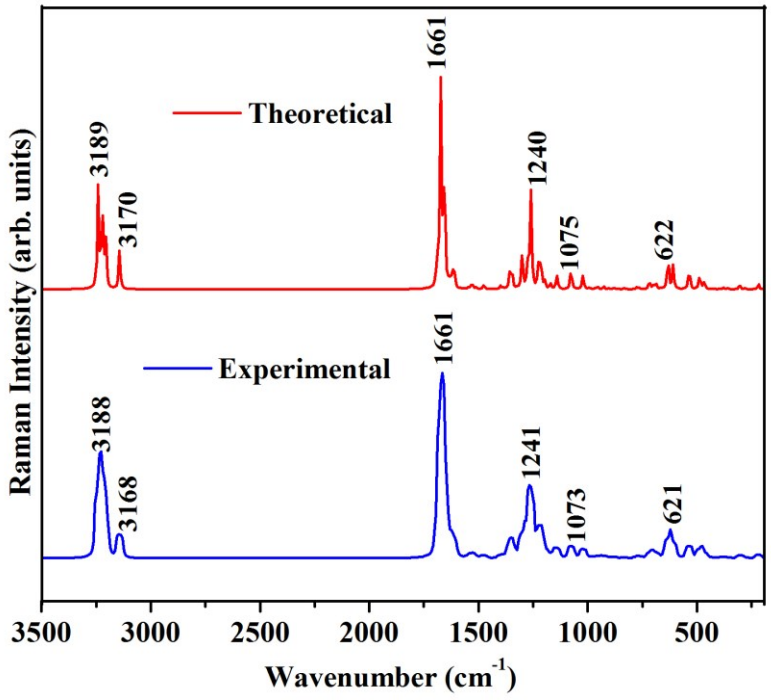

Fig.3. The simulated and observed Raman spectra of CMAQ molecule.

Table 2. The calculated vibrational frequencies (cm^{-1}), IR intensities (Km mol^{-1}), Raman scattering activity ($Å^4$ amu^{-1}), reduced mass (amu), force constants (mDyne/$Å^{-1}$) and vibrational assignments based on PED calculations for the CMAQ molecule.

Mode No.	Observed Wavenumber (cm^{-1})		Wavenumber (cm^{-1})		IR Intensity (Km mol^{-1})	Raman scattering activity ($Å^4$ amu^{-1})	Reduced Mass (amu)	Force Constant (mDyne/ $Å^{-1}$)	Assignment with PED (%)
	FT-IR	FT-Raman	Calculated	Scaled					
1			29	29	1.5531	4.9025	8.7513	0.0046	Skeletal motion (67%)
2			39	39	2.4820	4.1986	8.4251	0.0079	Ring torsion (56%)
3			72	71	5.1647	1.4670	9.7778	0.0301	Ring torsion (54%)
4			123	121	0.4505	0.5016	4.5389	0.0408	Skeletal motion (56%)
5			139	137	0.7411	4.4936	6.2625	0.0720	Skeletal motion (48%)
6			163	160	3.7113	0.4577	9.1138	0.1430	Ring torsion (54%)
7			187	184	2.4838	0.6150	3.6660	0.0756	Ring torsion (45%)
8			218	215	0.7725	9.2904	6.3482	0.1790	Ring torsion (42%)
9			278	273	0.3578	1.7215	5.0534	0.2306	Skeletal motion (34%)
10			303	298	0.2142	8.2182	6.6535	0.3617	Skeletal motion (44%)
11			357	351	7.4934	1.2949	4.3312	0.3255	Skeletal motion (43%)
12			377	371	0.4103	2.2664	5.3764	0.4522	Skeletal motion (41%)
13			394	387	39.8363	0.6052	10.3876	0.9505	C=O in plane bending (87%)
14			424	418	0.6125	0.8750	3.4119	0.3629	Skeletal motion (42%)
15			441	434	0.3751	0.5929	5.8367	0.6690	Skeletal motion (43%)
16			461	454	2.6271	5.5638	4.7588	0.5980	Ring torsion (42%)
17			470	462	2.9699	9.7451	3.5578	0.4631	Ring deformation (35%)
18			487	479	0.3947	25.7645	11.0552	1.5477	Ring deformation (34%)
19			535	527	19.3150	39.4447	5.5247	0.9337	C-H out of plane bending (56%)
20			608	599	22.3104	41.9493	6.3793	1.3930	Ring deformation (41%)
21		621m	632	622	44.0555	61.7566	5.7053	1.3465	C-Cl stretch/Skeletal motion(67%)
22			662	651	3.9005	2.1417	6.7509	1.7448	Skeletal motion (34%)
23			688	677	13.5580	11.9871	6.2725	1.7521	Skeletal motion (53%)
24	687w		701	690	37.3212	5.8941	3.5142	1.0181	C-H out of plane bending (67%)

Table 2. (Continued)

Mode No.	Observed Wavenumber (cm^{-1})		Wavenumber (cm^{-1})		IR Intensity (Km mol^{-1})	Raman scattering activity ($Å^4$ amu^{-1})	Reduced Mass (amu)	Force Constant (mDyne/ $Å^{-1}$)	Assignment with PED (%)
	FT-IR	FT-Raman	Calculated	Scaled					
25			717	705	0.2062	15.9474	6.5386	1.9815	Skeletal motion (51%)
26	740m		746	734	46.0763	0.5888	2.7108	0.8904	C-H out of plane bending (61%)
27			764	752	1.8731	3.1454	4.1304	1.4225	C-H out of plane bending (58%)
28			775	763	4.7018	3.4711	4.5901	1.6263	C-H out of plane bending (63%)
29			830	817	13.1095	2.6417	1.7627	0.7167	C-H out of plane bending (77%)
30			857	843	0.6746	0.3119	3.0142	1.3057	C-H out of plane bending (71%)
31			878	864	1.7136	3.5126	5.7333	2.6063	Ring skeleton (67%)
32			902	888	14.9081	1.3941	1.6236	0.7793	C-H out of plane bending (71%)
33			926	911	0.3225	6.2285	1.5834	0.8013	CH_2 torsion (56%)
34			951	936	0.5021	3.1327	1.4817	0.7902	C-H out of plane bending (87%)
35	946m		961	946	63.1653	2.8226	6.6170	3.6060	C-C Stretch/ C-H in plane bending (68%)
36			990	974	5.4588	3.1679	1.5631	0.9036	C-H out of plane bending (75%)
37			1020	1004	23.8504	28.1643	3.6073	2.2149	C-C Stretch/ C-H in plane bending (64%)
38			1028	1012	2.5023	0.6761	1.3921	0.8678	C-H out of plane bending (71%)
39			1036	1020	1.6920	0.9814	1.4008	0.8869	C-H out of plane bending (77%)
40			1053	1036	0.0026	0.3940	1.3854	0.9056	C-H out of plane bending (71%)
41	1073w		1075	1058	0.2160	43.6973	2.0194	1.3759	C-H in plane bending (69%)
42			1134	1116	2.1052	5.1113	2.8066	2.1279	C-H in plane bending (66%)
43			1142	1124	1.9458	27.9488	2.1175	1.6284	C-H in plane bending (67%)
44			1170	1151	6.1021	10.2456	1.2570	1.0145	CH_2 torsion (54%)
45			1197	1177	13.8495	14.2244	1.4641	1.2360	C-H in plane bending (61%)
46			1214	1195	14.2275	68.5300	1.7813	1.5490	C-H in plane bending (64%)
47			1225	1206	6.3042	44.2492	1.3250	1.1729	C-H in plane bending (76%)

Table 2. (Continued)

Mode No.	Observed Wavenumber (cm^{-1})		Wavenumber (cm^{-1})		IR Intensity (Km mol^{-1})	Raman scattering activity ($Å^4$ amu^{-1})	Reduced Mass (amu)	Force Constant (mDyne/ $Å^{-1}$)	Assignment with PED (%)
	FT-IR	FT-Raman	Calculated	Scaled					
48	1241w		1260	1240	71.8882	209.6502	3.0565	2.8627	C-C stretch/C-H in plane bending (78%)
49			1274	1254	17.6299	46.4892	1.7317	1.6582	C-C stretch/C-H in plane bending

									(71%)
50			1300	1279	60.3915	81.7119	1.1487	1.1440	CH_2 out of plane bending (61%)
51			1325	1304	25.2306	1.3649	1.6101	1.6669	C-C stretch/C-H in plane bending (76%)
52	1322vs		1346	1325	572.8052	39.3604	6.3103	6.7454	C-C stretch/C-H in plane bending (79%)
53			1356	1334	1.9181	36.0453	2.1438	2.3246	C-C stretch/C-H in plane bending (75%)
54			1387	1365	31.7377	2.2368	8.1499	9.2401	C-C stretch/C-H in plane bending (78%)
55			1399	1376	0.6939	7.1914	8.5120	9.8177	C-C stretch (67%)
56			1474	1451	2.1164	9.8512	3.2704	4.1910	C-C stretch/C-H in plane bending (78%)
57			1511	1487	0.5707	3.9475	2.2665	3.0501	C-H in plane bending (56%)
58			1529	1504	3.5952	13.5239	1.1518	1.5874	CH_2 in plane bending (61%)
59			1532	1508	6.0143	0.7207	2.4538	3.3960	C-H in plane bending (71%)
60			1544	1519	4.9636	4.0951	2.6661	3.7467	C-C stretch/C-H in plane bending (74%)
61			1613	1587	18.2554	49.5592	8.0412	12.3289	C=O stretch/C-C stretch/C-H in plane bending (75%)
62			1620	1595	7.3945	23.1343	6.5439	10.1310	C-C stretch/C-H in plane bending (67%)
63	1608s		1633	1607	207.0301	18.4403	6.6686	10.4881	C=O stretch/C-C stretch/C-H in plane bending (73%)

Table 2. (Continued)

Mode No.	Observed Wavenumber (cm^{-1})		Wavenumber (cm^{-1})		IR Intensity (Km mol^{-1})	Raman scattering activity ($Å^4$ amu^{-1})	Reduced Mass (amu)	Force Constant (mDyne/ $Å^{-1}$)	Assignment with PED (%)
	FT-IR	FT-Raman	Calculated	Scaled					
64			1656	1629	5.6478	289.6648	5.9930	9.6851	C-C stretch/C-H in plane bending (78%)
65			1672	1645	5.5695	468.8918	9.8568	16.2473	C=O stretch/C-C stretch/C-H in plane bending (79%)
66	1661m	1661vs	1689	1661	54.7687	57.1403	8.7506	14.7079	C=O stretch/C-C stretch/C-H in plane bending (89%)
67			3142	3092	11.6336	125.3332	1.0567	6.1480	CH_2 symmetric stretch (97%)
68			3206	3154	4.0736	78.0113	1.0871	6.5842	C-H stretch (98%)
69			3207	3156	7.2446	85.4060	1.0904	6.6103	C-H stretch (98%)
70			3218	3166	3.0951	62.9348	1.1110	6.7789	CH_2 asymmetric stretch (98%)
71		3168m	3221	3170	14.4972	177.1306	1.0915	6.6743	C-H stretch (98%)
72			3225	3173	2.2186	41.8383	1.0919	6.6917	C-H stretch (98%)
73			3237	3185	0.8275	35.2887	1.0929	6.7480	C-H stretch (98%)
74			3240	3188	6.8017	52.3485	1.0938	6.7664	C-H stretch (98%)
75	3187w	3188vs	3241	3189	14.6401	269.7379	1.0965	6.7876	C-H stretch (98%)

3.3 UV-Visible analysis

The electronic absorption spectrum of the CMAQ molecule was calculated in ethanol solution using the TD-DFT/B3LYP/cc-pVTZ level of theory, and the results are compared with experimental UV-Vis data in Table 3. The simulated and observed UV-Vis spectra of CMAQ is shown in Fig.4. The simulated spectrum (Fig. 4) shows a prominent electronic transition at 370 nm (3.35 eV) with a moderate oscillator strength (f = 0.2141), which corresponds predominantly to a HOMO → LUMO excitation (93%). This transition is assigned to an n → π* type excitation, involving promotion of a non-bonding electron from the carbonyl oxygen to the π* orbital of the anthraquinone framework. Experimentally, the absorption maximum is observed at 378 nm (3.28 eV), showing excellent agreement with the computed value, with only a small deviation of ~8 nm, which falls within the expected accuracy of TD-DFT calculations in polar solvents. The strong absorption band in this region is characteristic of anthraquinone derivatives, as reported in previous studies, where the n → π* transitions of the conjugated carbonyl chromophores dominate the visible absorption region [22]. The close correlation between theory and experiment not only validates the computational approach but also confirms the assignment of the electronic transitions. The HOMO–LUMO excitation highlights the role of conjugated π-systems in stabilizing the excited states and underlines the importance of the carbonyl substituents in modulating the spectral properties of CMAQ. Thus, the combined TD-DFT and experimental UV–Vis analysis establishes the electronic structure and optical activity of the CMAQ molecule with high reliability.

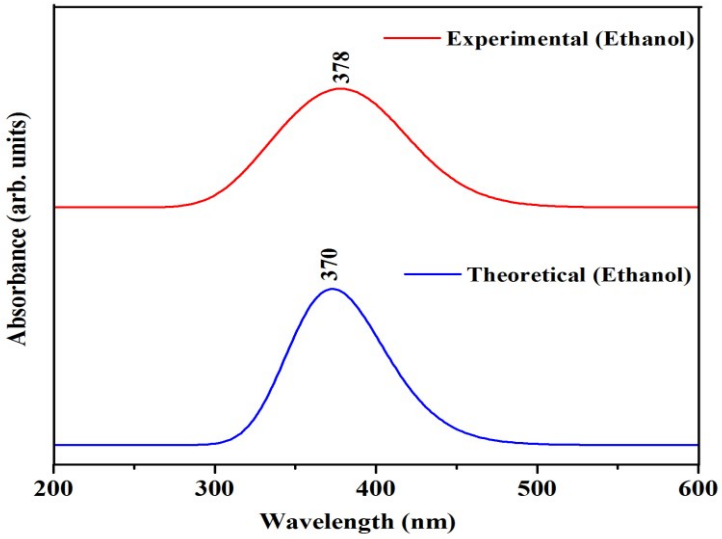

Fig.4. UV-Vis spectra of CMAQ molecule

Table 3. The calculated and observed UV-Vis spectral parameters in ethanol solution for CMAQ molecule with its assignments.

Calculated				Observed		Assignment
λ (nm)	E (eV)	F	Orbital contribution	λ (nm)	E (eV)	
370	3.35	0.2141	H→L (93%)	378	3.28	n→π*

3.4 Frontier molecular orbitals (FMOs) analysis

Frontier Molecular Orbitals (FMOs), namely the Highest Occupied Molecular Orbital (HOMO) and the Lowest Unoccupied Molecular Orbital (LUMO), play a pivotal role in determining the chemical reactivity, kinetic stability, and electronic properties of a molecule [23]. In this study, the FMO energies of the CMAQ molecule were computed using the B3LYP/cc-pVTZ level of theory. The FMOs of CMAQ is shown in Fig.5. The corresponding values, along with various global reactivity descriptors derived from them, are presented in Table 4. The energy of the HOMO was calculated to be −7.17 eV, while the LUMO energy was found to be −2.99 eV, resulting in a HOMO–LUMO energy gap (ΔE) of 4.18 eV. This moderately large energy gap indicates a relatively stable molecular system with low chemical reactivity under ambient conditions. However, the presence of a chloromethyl substituent may provide reactive sites, facilitating interaction with electrophilic or nucleophilic species.

The ionization energy (I) and electron affinity (A) were calculated based on Koopmans' theorem as 7.17 eV and 2.99 eV, respectively, corresponding to the negative values of the HOMO and LUMO energies. These values indicate that CMAQ possesses moderate electron-donating and electron-accepting capabilities, important characteristics for designing molecules with charge transfer or electron transport functionalities. The global hardness (η) of the molecule was determined to be 2.09 eV, reflecting its resistance to deformation or polarization of the electron cloud under small perturbations. In contrast, the global softness (S) was calculated as 0.48 eV^{-1}, implying a moderate tendency of the molecule to participate in soft-soft interactions according to Pearson's Hard-Soft Acid-Base (HSAB) theory.

The chemical potential (μ), a measure of the escaping tendency of electrons from equilibrium, was found to be −5.08 eV, suggesting a favorable electronic distribution and moderate electronegativity. The electrophilicity index (ω) of 6.17 eV further supports the molecule's ability to accept electrons from nucleophilic environments, thus establishing CMAQ as a promising candidate for electrophilic interaction-driven applications, such as in bio-conjugation or charge transfer complexes. These FMO-based descriptors provide a comprehensive picture of the electronic structure of CMAQ, underscoring its stability, moderate reactivity, and potential use in molecular electronics, photochemical systems, and pharmaceutical scaffold design.

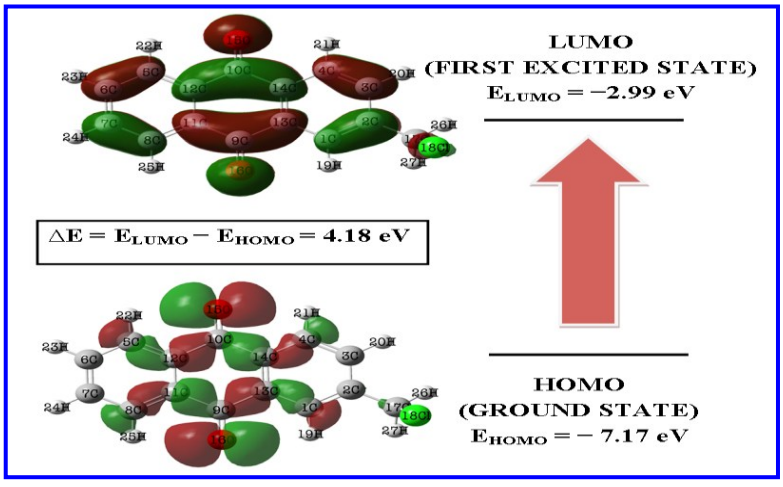

Fig.5. FMOs of CMAQ molecule

Table 4. The calculated FMOs and related molecular properties of the CMAQ molecule.

Molecular properties	Energy (eV)
E_{HOMO} (eV)	−7.17
E_{LUMO} (eV)	−2.99
Energy gap (eV)	4.18
Ionization energy (I)	7.17
Electron Affinity (A)	2.99
Global hardness (η)	2.09
Softness (S)	0.48
Chemical potential (μ)	5.08
Electrophilicity index (ω)	6.17
Energy gap = $E_{LUMO} - E_{HOMO}$; I = $-E_{HOMO}$; A = $-E_{LUMO}$; η = ½ ($E_{LUMO} - E_{HOMO}$); S = 1/η; μ = ½ ($E_{LUMO} + E_{HOMO}$); ω = μ^2 /2η.	

3.5 Mulliken atomic charge distribution analysis

The Mulliken atomic charge distribution of the CMAQ molecule (Fig. 6) reveals pronounced polarization across the molecular framework [24]. The carbonyl oxygen atoms O15 (−0.407) and O16 (−0.408) carry the most significant negative charges, highlighting their strong electron-withdrawing nature and their potential role as hydrogen-bond acceptors. The corresponding carbonyl carbons C9 (+0.190) and C10 (+0.189) are markedly positive, indicating electrophilic sites prone to nucleophilic attack, which is consistent with the observed strong IR bands in the C=O stretching region. Most aromatic carbons (C1, C3–C8) bear small negative charges (−0.12 to −0.16 e), whereas C11–C14 exhibit slight positive values (+0.06), reflecting delocalized π-electron distribution influenced by the adjacent carbonyl groups. The chlorine substituent (Cl18) carries a weakly negative charge (−0.067), in line with its electronegativity, while C17 shows a large negative charge (−0.491), suggesting enhanced local electron density, though this anomaly may reflect the known basis-set dependence of Mulliken analysis. As expected, all hydrogen atoms are positively charged, with H26 (+0.205) and H27 (+0.209) appearing more electropositive due to their bonding environment. Thus, the Mulliken population analysis indicates that the carbonyl groups dominate the charge distribution of CMAQ, governing its electronic structure, spectroscopic behavior, and likely sites of intermolecular interactions.

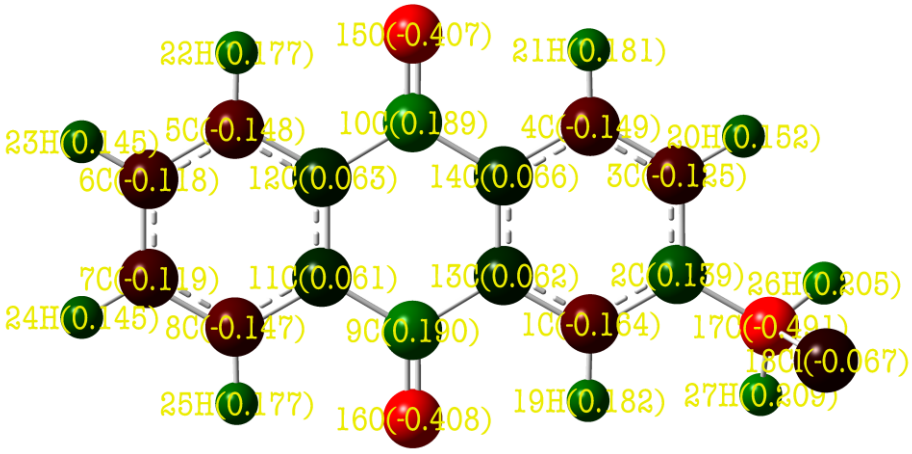

Fig.6. Mulliken atomic charge distribution of CMAQ molecule

3.6 Molecular Electrostatic Potential (MEP) Surface Analysis

The Molecular Electrostatic Potential (MEP) surface of CMAQ, calculated at the B3LYP/cc-pVTZ level of theory, provides crucial insights into the charge distribution and reactive regions of the molecule [25]. MEP surface of CMAQ is shown in Fig.7. The MEP map reveals that the most electron-rich regions (indicated by red color) are localized around the two carbonyl oxygen atoms of the anthraquinone core, marking them as the most favorable sites for electrophilic attack due to their high electron density. In contrast, the chloromethyl group, particularly the carbon bonded to chlorine, displays significant electron deficiency (blue regions), suggesting its susceptibility to nucleophilic attack. This electron-withdrawing effect of the chlorine atom also contributes to the polarization of the electron density across the aromatic ring system. The MEP surface further illustrates a moderately delocalized electrostatic potential over the anthraquinone skeleton, which is indicative of its extended π-conjugation and aromatic stability. Such distribution is important for understanding the molecule's interaction potential, including hydrogen bonding and π-π stacking in supramolecular or biological environments. Overall, the MEP analysis complements the FMO results and highlights the reactive hot spots in CMAQ, which may influence its chemical behavior and interaction with biomolecular targets.

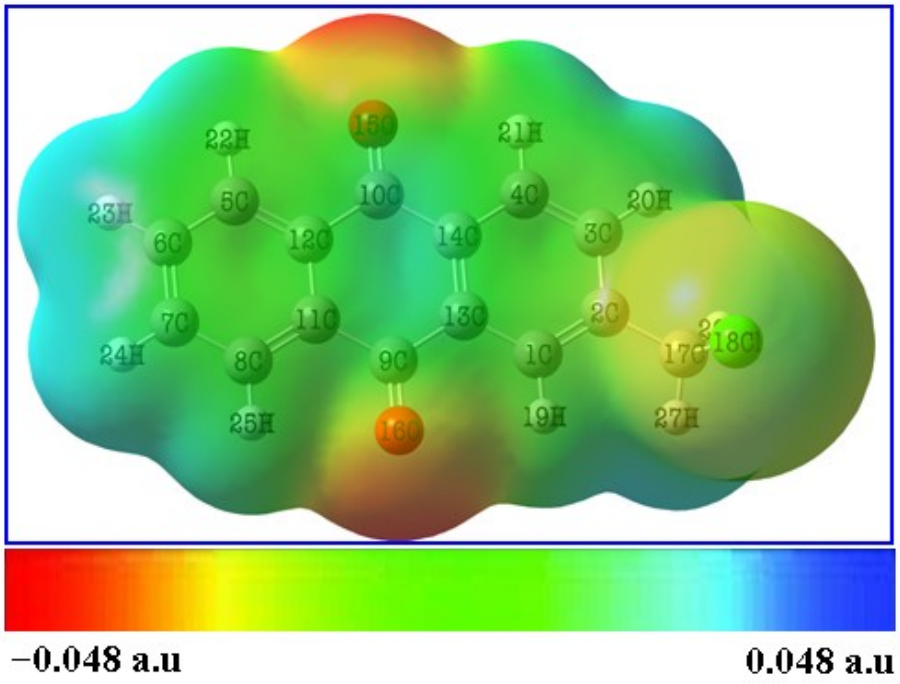

Fig. 7. Molecular Electrostatic Potential Surface of CMAQ molecule

3.7 Molecular docking Analysis

Molecular docking simulations were conducted to investigate the binding interactions of the CMAQ molecule with two cancer-related proteins, Dipeptidyl Peptidase-4 (DPP-4; PDB ID: 2ONC) and p38α Mitogen-activated Protein Kinase (MAPK14; PDB ID: 3FMK), in order to rationalize its selective cytotoxic activity [25,26]. The docking poses of the corresponding proteins with the ligand is depicted in Fig.8. CMAQ demonstrated a stronger binding affinity toward DPP-4 with a docking score of −7.42 kcal/mol compared to −6.21 kcal/mol for p38α MAPK, suggesting that the DPP-4 binding pocket provides a more favorable environment for ligand accommodation. A closer inspection of the interaction profile revealed that within the DPP-4 active site, CMAQ formed hydrogen bonds with GLY424 (3.2 Å) and TYR381 (2.6 Å), while additional hydrophobic contacts further stabilized the ligand orientation and reinforced the overall complex stability. Conversely, in the p38α MAPK binding cavity, CMAQ established hydrogen bonds with LYS53 (1.9 Å), ALA34 (2.2 Å), and ASP168 (2.8 Å); however, despite the presence of multiple hydrogen bonds, the overall docking score was weaker, reflecting a less stable interaction and suboptimal complementarity with the binding site. These computational observations are in strong agreement with the experimental cytotoxicity assays, where CMAQ exhibited greater potency against A549 lung cancer cells, correlating with its stronger interaction and stabilization within the DPP-4 active site, while the weaker binding to p38α MAPK was consistent with its reduced cytotoxic effect toward HeLa cervical cancer cells.

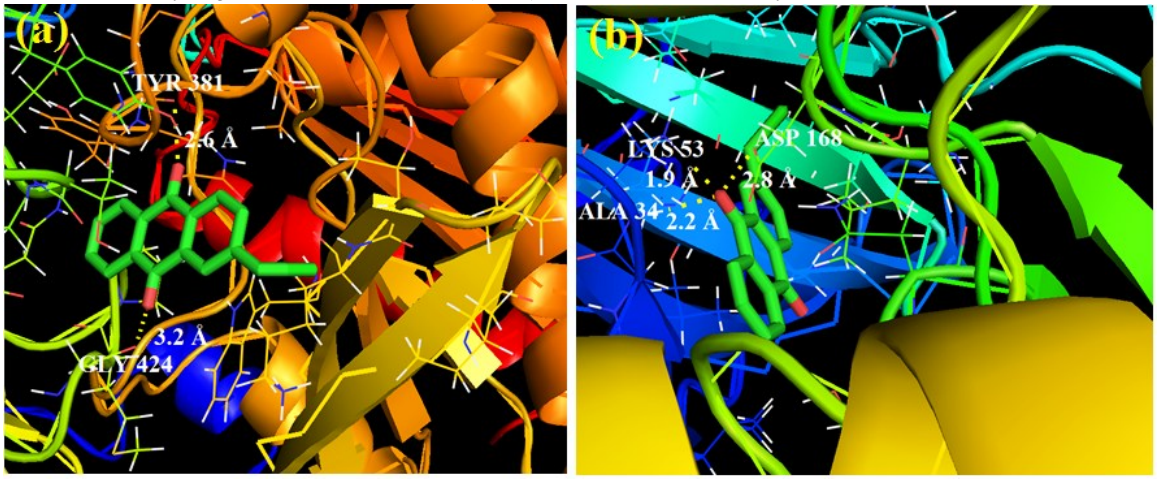

Fig. 8. The lowest energy docked poses of the CMAQ ligand with targeted proteins including (a) Dipeptidyl Peptidase-4 (DPP-4) [PDB ID: 2ONC] and (b) p38α Mitogen-activated protein kinase 14 (p38α MAPK) [PDB ID: 3FMK]

3.8 In Vitro Cytotoxicity Anticancer Studies

3.8.1 MTT Assay

The cytotoxic potential of the CMAQ molecule was investigated against A549 (lung cancer) and HeLa (cervical cancer) cell lines using the MTT assay [26]. Cells were treated with a range of CMAQ concentrations (0–360 µg/mL) for 24 hours, and cell viability was quantified to determine its anticancer efficacy. The results, presented in Fig. 9 for A549 cells and Fig. 10 for HeLa cells, clearly show a concentration-dependent decrease in cell viability, confirming the dose-dependent cytotoxic nature of CMAQ.

For A549 lung cancer cells, a marked reduction in viability was observed even at relatively low concentrations. A gradual decrease began around 75 µg/mL, with a sharp decline evident

at 150 µg/mL. At 300 µg/mL, the majority of A549 cells were non-viable, and at the highest concentration (360 µg/mL), cell survival was reduced to below 10%. The calculated IC_{50} value of 4.12 µg/mL reflects the strong cytotoxic activity of CMAQ against A549 cells. This potent effect correlates well with the molecular docking results, where CMAQ displayed a higher binding affinity (−7.42 kcal/mol) with the DPP-4 protein (PDB ID: 2ONC), reinforcing its selective efficacy toward lung cancer cells.

In the case of HeLa cervical cancer cells, cytotoxicity was less pronounced at lower doses (75–225 µg/mL), with only moderate reductions in viability. A clear decrease was observed at the 300 µg/mL range, and at 360 µg/mL, cell survival declined to below 18%. The IC_{50} value was determined to be 13.25 µg/mL, indicating moderate cytotoxic potential compared to A549 cells. This observation aligns with docking studies, where CMAQ exhibited a weaker binding affinity (−6.21 kcal/mol) toward the p38α MAPK protein (PDB ID: 3FMK), suggesting reduced inhibitory activity against cervical cancer.

The enhanced sensitivity of A549 cells to CMAQ treatment may be attributed to the stronger hydrogen bonding and hydrophobic interactions within the DPP-4 binding site, which plays a vital role in regulating cancer cell proliferation and apoptosis. In contrast, weaker interactions with p38α MAPK in HeLa cells correlate with the higher IC_{50} value and reduced susceptibility. Morphological examinations further supported these findings, as both A549 and HeLa cells exhibited typical apoptotic features after CMAQ exposure, including cell shrinkage, detachment, membrane blebbing, and nuclear condensation (Fig. 11).

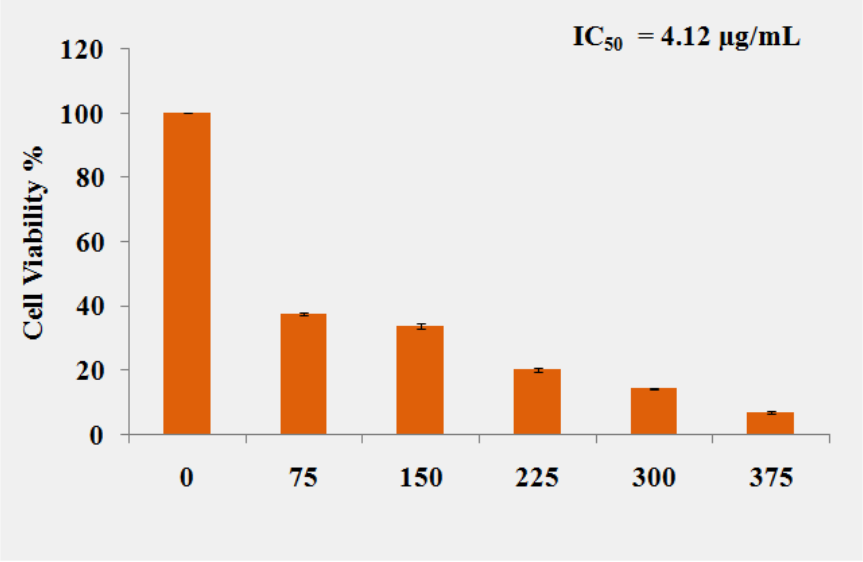

Fig. 9. MTT assay measurement on different percentages of cell viability in A549 Lung cancer cell lines against varied concentrations of CMAQ compound.

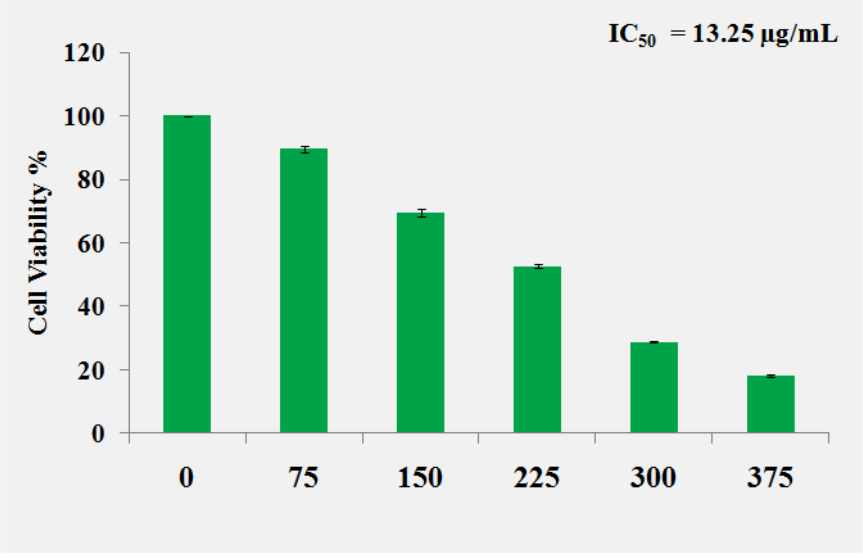

Fig.10. MTT assay measurement on different percentages of cell viability in HeLa cervical cancer cell lines against varied concentrations of CMAQ compound.

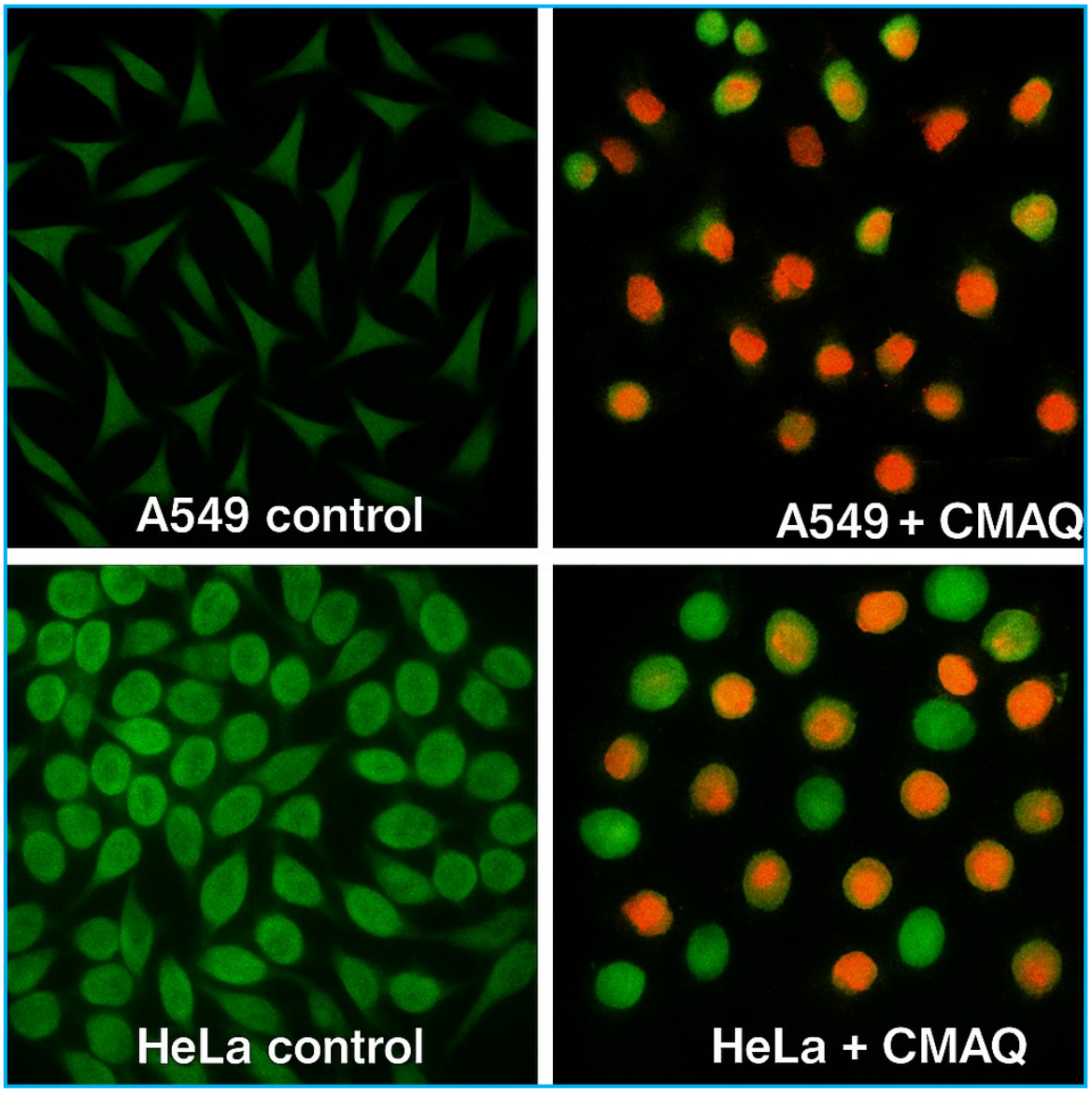

Fig. 11. Morphological profile of the A549 Lung cancer cells (a) control and (b) after treated with DAAQ compound for 24 hours and the morphological profile of the HeLa Cervical cancer cells (c) control and (d) after treated with CMAQ compound for 24 hours.

CONCLUSION

This study provided an integrated spectroscopic, theoretical, and biological evaluation of 1-(Chloromethyl)anthraquinone (CMAQ) to establish its molecular properties and anticancer potential. DFT-based structural optimization confirmed a stable anthraquinone framework with significant π-electron delocalization, while vibrational and UV–Vis spectral analyses validated the computational predictions through excellent agreement with experimental data. Electronic property evaluations identified carbonyl oxygens and the chloromethyl substituent as key reactive centers, supported by Mulliken charge distribution and MEP surface analysis. Molecular docking studies revealed that CMAQ exhibits preferential binding to DPP-4 with a docking score of −7.42 kcal/mol, stabilized by hydrogen bonds with GLY424 and TYR381, whereas weaker interactions were observed with p38α MAPK (−6.21 kcal/mol). These theoretical insights correlated strongly with biological assays, where CMAQ showed potent cytotoxicity against A549 lung cancer cells (IC_{50} = 4.12 µg/mL) and comparatively reduced activity against HeLa cervical cancer cells (IC_{50} = 13.25 µg/mL). Morphological studies further confirmed apoptosis-like features such as cell shrinkage, blebbing, and nuclear condensation upon treatment. Collectively, these results suggest that CMAQ exerts selective anticancer activity through strong stabilization within the DPP-4 active site, supporting its candidacy as a potential lead molecule for lung cancer therapy.

Acknowledgements

The authors extend their sincere gratitude to the college management for their support and for granting permission to perform this research. Dr. R. Premkumar also extends his gratitude to the management of Nadar Mahajana Sangam S. Vellaichamy Nadar College for granting access to the Advanced Materials Research Centre in the PG and Research Department of Physics, which was instrumental in this study. Additionally, heartfelt thanks are extended to SAIF at IIT-Madras for their assistance in recording the FT-IR, FT-Raman, and UV-Vis spectra of the sample.

REFERENCES

- Ghosh, S.; Jana, P. K.; Mukherjee, S. (2016) Theoretical studies on substituted anthraquinones: Structure, conjugation, and electronic effects. Computational and Theoretical Chemistry, 1094, 1–9.
- Khan, M. S.; Kumar, S.; Choudhury, A. R. (2017) Structural, electronic, and vibrational study of anthraquinone derivatives: A DFT approach, Journal of Molecular Structure, 1134, 469–478.
- Bolton, J. L.; Dunlap, T (2017) Formation and biological targets of quinone methides, Chemical Research in Toxicology, 30(1), 13–37.

- Koyama, J.; Morita, I.; Kobayashi, N.(2008).Antitumor anthraquinones from Rubia cordifolia and their biological activities, Planta Medica, 74(13), 1494–1496.
- Srinivas, U. S.; Tan, B. W. Q.; Vellayappan, B. A.; Jeyasekharan, A. D. (2019)ROS and the DNA damage response in cancer, Oncogene, 38(32), 6589–6604.
- Ramesh, V.; Ravindran, R. (2020).Photophysics and photochemistry of anthraquinones: Potential in photodynamic therapy, Journal of Photochemistry and Photobiology B: Biology, 204, 111791.
- Parisini, E.; Metrangolo, P.; Pilati, T.; Resnati, G.; Terraneo, G. (2011) Halogen bonding in halocarbon–protein complexes: A structural survey.Chemical Society Reviews, 40(5), 2267–2278.
- Xu, Z.; Yang, Z.; Liu, Y.; Lu, Y.; Chen, Y.; Zhao, Y (2019) Halogen bonding for rational drug design and new drug discovery, Angewandte Chemie International Edition, 58(48), 16760–16763.
- Scott, A. P.; Radom, L (1996) Harmonic vibrational frequencies: An evaluation of Hartree–Fock, Møller–Plesset, quadratic configuration interaction, density functional theory, and semiempirical scale factors, Journal of Physical Chemistry, 100(41), 16502–16513.
- Socrates, G (2001) Infrared and Raman Characteristic Group Frequencies: Tables and Charts. 3rd Ed.; Wiley: Chichester, UK.
- Morris, G. M.; Huey, R.; Lindstrom, W.; et al. (2009). AutoDock4 and AutoDockTools4: Automated docking with selective receptor flexibility. Journal of Computational Chemistry, 30(16), 2785–2791.
- Ferreira, L. G.; Dos Santos, R. N.; Oliva, G.; Andricopulo, A. D. (2015) Molecular docking and structure-based drug design strategies, Molecules, 20(7), 13384–13421.
- Mosmann, T (1983) Rapid colorimetric assay for cellular growth and survival: Application to proliferation and cytotoxicity assays. Journal of Immunological Methods, 65(1–2), 55–63.
- Frisch, M. J.; Trucks, G. W.; Schlegel, H. B.; et al. (2013). Gaussian 09, Revision D.01. Gaussian, Inc., Wallingford CT, USA.
- Scott, A. P.; Radom, L (1996). Harmonic vibrational frequencies: An evaluation of Hartree–Fock, Møller–Plesset, quadratic configuration interaction, density functional theory, and semiempirical scale factors, Journal of Physical Chemistry, 100(41), 16502–16513.
- Jamróz, M. H. (2004) Vibrational Energy Distribution Analysis (VEDA): Program for analysing vibrational modes, Spectrochimica Acta Part A: Molecular and Biomolecular Spectroscopy, 114, 220–230.
- Dennington, R.; Keith, T.; Millam, J (2009) GaussView, Version 5.* Semichem Inc., Shawnee Mission, KS, USA.
- Pargellis, C.; Tong, L.; Churchill, L.; Cirillo, P. F.; Gilmore, T.; Graham, A. G.; Grob, P. M.; Hickey, E. R.; Moss, N.; Pav, S.; Regan, J. (2002). Inhibition of p38 MAP kinase by selective small molecules: Novel binding mode revealed by X-ray crystallography, Journal of Biological Chemistry, 277(13), 11140–11148.
- T. Valarmathi, R. Premkumar, A. Milton Franklin Benial (2020) Spectroscopic and molecular docking studies on 1-Hydroxyanthraquinone: A potent ovarian cancer drug, Journal of Molecular Structure, 1213 (2020) 128163.
- T. Valarmathi, R. Premkumar, M.R. Meera, A. Milton Franklin Benial (2021) Spectroscopic, Quantum Chemical and Molecular Docking Studies on 1-Amino-5-chloroanthraquinone: A Targeted Drug Therapy for Thyroid Cancer, Spectrochim. Acta 255(3) 119659.
- R. Premkumar, Shamima Hussain, Stève-Jonathan Koyambo-Konzapa, Naidu Dhanpal Jayram, M.R. Meera, T. Mathavan (2021) SERS and DFT Studies of 2-(Trichloroacetyl)pyrrole chemisorbed on the Surface of Silver and Gold Coated Thin Films: In Perspective of Biosensor Applications, A. Milton Franklin Benial, Journal of Molecular Recognition, e2921.
- R. Premkumar, Shamima Hussain, Stève-Jonathan Koyambo-Konzapa, Naidu Dhanpal Jayram, T. Mathavan, A. Milton Franklin Benial (2021) SERS and DFT Investigations of Methyl 4-bromo-1H-pyrrole-2-carboxylate adsorbed on Silver and Gold Substrates: In Perspective of Biosensor Applications, , Journal of Molecular Structure, 1236 130272.
- G. Pandimeena, R. Premkumar, T. Mathavan, A. Milton Franklin Benial (2021) Spectroscopic, Quantum chemical and Molecular docking Studies on Methyl 6-aminopyridine-3-carboxylate: A potent bioactive agent for the treatment of sarcoidosis, Journal of Molecular Structure, 1231, 129996.
- Noreen Akram, Asim Mansha, R. Premkumar, A. Milton Franklin Benial, Sadia Asim , Shahzad Zafar Iqbal, Hafiz Saqib Ali, Spectroscopic, quantum chemical and molecular docking studies on 2,4-dimethoxy-1,3,5-triazine: a potent inhibitor of protein kinase CK2 for the development of breast cancer drug, Molecular Simulation, 46 (2020) 1340-1353.
- M. Ramuthai, S. Jeyavijayan, R. Premkumar, M. Uma Priya, Naidu Dhanpal Jayram (2021) Structure, Spectroscopic Investigation, Molecular docking and In vitro Cytotoxicity Studies on 4,7-dihydroxycoumarin: A breast cancer drug, , Journal of Computational Biophysics and Chemistry, 21, 219-236.
- R. Geetha, M.R. Meera, C. Vijayakumar, R. Premkumar, A. Milton Franklin Benial (2022) Synthesis, Spectroscopic Characterization, Molecular docking and In Vitro Cytotoxicity Investigations on 8-Amino-6-Methoxy Quinolinium Picrate: A novel breast cancer drug, Journal of Biomolecular Structure and Dynamics, 10.1080/07391102.2021.2024259.